

## Supplementary Materials: High Fidelity Volumetric Additive Manufacturing

### S1. Resin chemistry and photopolymerization

With the choice of resin chemistry in this work, the majority of the light dose is accumulated in the induction period before resin gelation. Note that gelation occurs when the prepolymer's density begins to increase and the storage modulus of the medium exceeds its loss modulus. During the oxygen induction period, the optical dose generates free radicals that primarily react with molecular oxygen dissolved in the prepolymer. Only after sufficient  $O_2$  depletion can the photopolymerization begin. For low to moderate intensity (as in this case), the number of free radicals generated during the induction period is linearly proportional to dose, where dose is the product of intensity and exposure time [22]. In the current work, we use a constant rotation rate and do not attempt to change the illumination intensity across successive rotations of the print vial. Thus, we may express the dose distribution as a product of the number of rotations  $N_r$  and the dose deposited in a single rotation. There may potentially be some benefit to modifying the exposure recipe over the course of successive rotations in order to accommodate non-linearities and the diffusion of chemical species. The non-linearities primarily arise from the photopolymerization process (as opposed to the induction phase). We have proceeded with the constant-rotation-rate method in this work since the induction phase consumes a large fraction (80-90%) of the dose for this chemistry.

We further assume that the high viscosity of the resin used in experimentation significantly limits free radical and  $O_2$  diffusion. Diffusivities of  $O_2$  on the order of  $10^{-4}$ - $10^{-6}$  cm<sup>2</sup>/s in monomers and other organic liquids with viscosities on the order of 1-50 cP have been reported [23, 24, 25]. The diffusion rate for small molecules in liquids of high molecular weight is proportional to the  $-2/3$  power of the liquid's viscosity [26] which means that the high viscosity monomer used in this work (100,000 cP; see Section 6.3) has  $O_2$  diffusivity on the order of  $10^{-8}$  cm<sup>2</sup>/s. The characteristic diffusion length over a 500 s print time (similar to prints in this work) is 10  $\mu$ m, which is smaller than the expected minimum feature size ( $\sim 500$   $\mu$ m) and also smaller than what is resolvable with the 3D optical metrology. Therefore, we have neglected the effect of oxygen diffusion in the forward model.

### S2. Discretization

DLP projectors have a fixed space-bandwidth product (etendue), as well as a temporal frame rate at which the video can be projected. This discretization needs to be accounted for in the forward model and the projection calculation. We consider how the spatial resolution, temporal frame rate and angular rotation rate of the vial determine the discretization of the projection space intensity from  $g(\rho, \theta, z)$  and the resulting 3D dose distribution  $f(\mathbf{r}, z)$ . We will represent the discretization of the continuous intensity  $g$  as  $G_{i,j,k}$  over a specific basis of the projection space  $(\rho, \theta, z)$ . The basis will be described in terms of the natural discretization of the projection space. This discretization will then inform the choice of sampling used in

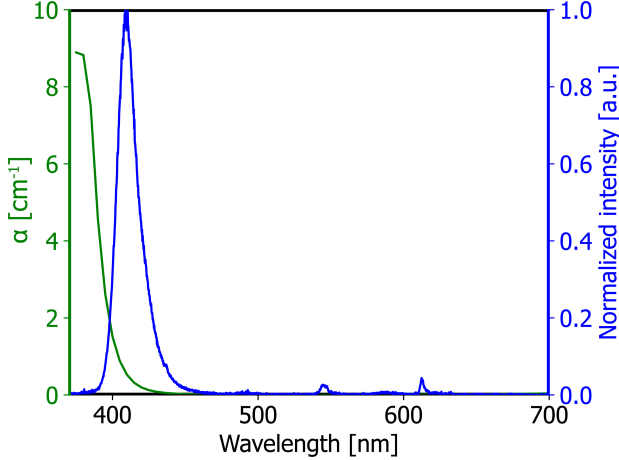


Figure S1: Absorption spectrum of the resin formulation in units of inverse length (left axis) and the normalized light intensity spectrum of the projector (right axis).

representing the inverse problem, so long as computational resources are not a constraint. The finite frame rate induces a discretization in the angular domain  $\theta$ .

If the maximum possible projector frame rate is  $f_p$  frames per second, the angular resolution is determined by the angle rotated during a single frame:  $\delta\theta = \Omega/f_p$ . It is possible to obtain improved angular resolution by rotating slowly and reducing the total number of rotations so as to maintain consistent total dosage. However, the fast angular rotation rate case provided sufficient angular resolution based on spatial frequency sampling arguments described in Kelly et al. (Supplementary Materials Fig. S15) [10]. In order to describe spatial discretization, we consider the image intensity distribution of a single projector pixel prior to resin attenuation. Consider a particular projector pixel, indexed by radial and height indices of the projector. When this is imaged into the resin volume, it results in a spatially continuous function  $\psi_0(\rho, z)$  where  $\rho$  is the radius variable along the vector  $\hat{\theta}$  corresponding to the instantaneous angle  $\theta$  of the projector. If we define this pixel function  $\psi_0$  as centered at the origin of the coordinate system along height and radius, the other pixels produce a response given by  $\psi_0(\rho - \rho_i, z - z_k)$ .  $\rho_i$  and  $z_k$  lie on a Cartesian grid along radius and height. Note that the height direction is parallel to the axis of rotation of the print medium. The intensity distribution resulting from a single pixel  $\psi_0$  is concentrated around  $\rho = 0$  due to finite pixel size, and is here defined for unity projector pixel intensity. Together with the spatial pixel resolution, the finite angular resolution imposes a projection space voxel given by:  $\phi_0(\rho, \theta, z) = \psi_0(\rho, z) \times b_{\delta\theta}(\theta)$  where  $b_{\delta\theta}(\theta)$  is a boxcar function in the angular domain (centered at 0 and with support of  $\delta\theta$ ). We can then express the continuous projection intensity function as a linear combination of the individual voxel basis functions, weighted by discrete projector intensities:

$$f(\rho, \theta, z) = \sum_{i,j,k} G_{i,j,k} \phi_{i,j,k}(\rho, \theta, z) \quad (\text{S1})$$

where  $\phi_{i,j,k}(\rho, \theta, z) = \phi_0(\rho - \rho_i, \theta - \theta_j, z - z_k)$ . The goal of the optimization is to determine a feasible solution

for the projector intensities  $G_{i,j,k}$  in energy flux units, subject to the physical constraints:

$$0 \leq G_{i,j,k} \leq G_{max} \quad (\text{S2})$$

where  $G_{max}$  is the maximum power of a projector pixel in  $W/cm^2$ . Constraints in print space  $(\mathbf{r}, z)$  are described in Section 3 below. In the calculation, we will also impose a target region voxelization, where the target geometry is treated in terms of discrete voxels. The target geometry voxels should ideally have 5 dimensions smaller than or equal to those imposed by the projection space voxel. This is in order to sample the real space dose distribution in a sufficiently dense manner while calculating the loss function and its gradient. However, it is possible that this is computationally infeasible, particularly given the large number of pixels available in modern projectors. We decided to sample the projector intensity at a coarse pixel size, 2-4× larger than the available pixel size. This was done in order to allow the calculation to be computationally 10 tractable on a personal laptop. With additional computational resources, it is likely that the full resolution of the projector can be used. In order to map the coarse projection intensities to the pixel, a conventional upsampling method was used. Due to the rather coarse representation of the problem, it is acceptable here to consider the ray optics limit in our forward model description as opposed to a wave-optics-based Abbe 15 image formation model. The ray optics model allows us to use the exponential Radon transform in our forward model description and accelerates the optimization procedure. In our comparison metrics, we have always compared the print geometries with the coarser representation that was used in order to initialize the problem. This is described in more detail in Section 4.

We also note some additional assumptions related to the aforementioned projection voxel basis functions. These assumptions help to simplify the calculation without affecting the accuracy of the forward model 20 significantly under the chosen physical settings of the problem. Firstly, we note that the basis function  $\psi_0(\rho, z)$  may be close to a simple boxcar function with finite support, but it will depend on the shape of the projector pixel, the color tiling scheme used by the DLP manufacturer as well as details of the optical system and resin optics, particularly the imaging modulation transfer function of the projector into the resin vial. A more physically accurate picture of the dose basis function is a ‘pixel spread function’ resulting from 25 the imaging of a DLP pixel into the exposure medium. This concern is nullified by our representation of the problem at a computational pixel size that is significantly coarser than permitted by hardware. Additionally, we also note that the diffraction tomography framework is more suitable for fully incorporating the scalar wave theory physics of this problem when it is treated close to the hardware pixel size [27]. However, the current ray optics picture allows us to neglect the angular dependence of the ‘pixel spread function’ in the 30 resin volume and treat it as an integral projection of a boxcar DLP projector pixel. Lastly, we have also assumed a perfect step-like transition in time as the frame changes, which allows the angular response to be approximated as a boxcar function  $b_{\delta\theta}(\theta)$ . A more precise approach would be to explicitly consider the rise and fall times of the projector pixel values and incorporate this in the angular integration formula of 2, assuming a constant angular rotation rate. While these concerns regarding the discretization and treatment

of the physics model are valid, they do allow a much simplified computational description. For instance, the simplification permits the use of fast-Fourier-transform-based packages for the Radon transform and inverse Radon transform in solving the inverse problem iteratively, which is especially important given the iterative approach. A fast Laplace-transform-based approach is also possible for the exponential Radon transform  
<sup>5</sup> [28].

### S3. Connection to heuristic gradient descent approach

We observe that the PM method generalizes the heuristic finite difference approach proposed by Kelly et al. Here we argue how the PM method is a superset of techniques from which the prior approach can be derived. In the previous heuristic method, the notion was that the projection space update should be  
<sup>10</sup> calculated by using a Radon transformation (integral projection) of the violating volumes at each iteration. The violating volumes were calculated for three perturbed gelation thresholds and the Radon transform was calculated on the mean of these violations. This led to a projection space update vector, which was used to change the projector weights at that iteration of optimization. If we denote the loss gradient in projection space as  $\frac{\partial \mathcal{L}}{\partial \mathbf{g}}$ , this Radon transform approach can be formalized by expressing the updating gradient as:

$$\frac{\partial \mathcal{L}}{\partial \mathbf{g}}(\rho, \theta, z) \sim -T_{-\alpha}[I_{viol}(\mathbf{r}, z)] \quad (\text{S3})$$

<sup>15</sup> where  $I_{viol}(\mathbf{r}, z)$  is an indicator function over the violating volumes in the print space and  $T_{-\alpha}$  denotes the exponential Radon transform ( $\sim$  indicates proportionality). The indicator function is 1 where we have undesirable excess dose and -1 where it is lower than desired (zero elsewhere). Now, performing an inner product in projection space  $\mathcal{P}$  using pixel basis functions  $\phi_{i,j,k}(\rho, \theta, z)$  yields the loss gradient for each pixel (substituting from equation S3):

$$\frac{\partial}{\partial G_{i,j,k}} \mathcal{L}[t] = \left\langle \phi_{i,j,k} \left| \frac{\partial \mathcal{L}}{\partial \mathbf{g}}(\rho, \theta, z) \right. \right\rangle_{\mathcal{P}} \sim -\langle \phi_{i,j,k} | T_{-\alpha} | I_{viol}(\mathbf{r}, z) \rangle_{\mathcal{P}} \quad (\text{S4})$$

<sup>20</sup> where  $\langle \cdot \rangle_{\mathcal{P}}$  is bra-ket notation for the inner product formed by integration in projection space. However, by definition of the Hermitian adjoint, we have the following identity:

$$\langle \phi_{i,j,k} | T_{-\alpha} | I_{viol}(\mathbf{r}, z) \rangle_{\mathcal{P}} = \langle I_{viol}(\mathbf{r}, z) | T_{-\alpha}^* | \phi_{i,j,k} \rangle_{\mathcal{R}} \quad (\text{S5})$$

where  $\langle \cdot \rangle_{\mathcal{R}}$  denotes the inner product formed by integration over real space  $(\mathbf{r}, z)$  and  $T_{-\alpha}^*$  denotes the exponential backprojection operation. It is easy to then confirm that the right hand side of equation S5 is proportional to the right hand side of equation 6:

$$\langle I_{viol}(\mathbf{r}, z) | T_{-\alpha}^* | \phi_{i,j,k} \rangle_{\mathcal{R}} = \int_{\sim V_1[t]} (T_{-\alpha}^*[\phi_{i,j,k}](\mathbf{r})) d\mathbf{r} - \int_{\sim V_2[t]} (T_{-\alpha}^*[\phi_{i,j,k}](\mathbf{r})) d\mathbf{r}. \quad (\text{S6})$$

<sup>25</sup> Since the loss gradients are proportional, the heuristic method in the previous demonstration by Kelly et al. [10] formalizes to the  $L_1$  penalty minimization approach proposed here. However, we note that the

previous optimization method was a heuristic: the idea of using the Radon transform of the violating volumes as the projection space update was based on the intuition that convergence would be obtained when there were no more violating volumes. Instead, expressing the problem in terms of an analytical loss function has very important practical as well as conceptual advantages. In terms of computation, the use of an analytical  
5 loss function, and its analytical gradient is well known to lead to much better convergence of mathematical optimization approaches. In fact, the use of the L-BFGS-B algorithm (discussed in Section 3.3) requires the use of an analytical gradient: the update step is very different from simple gradient descent. Secondly, expressing as a loss function allows us to explore precise dose constraints, as well as other loss functions. For instance, an  $L_2$  loss, or loss function incorporating other dose constraints, will not be mathematically  
10 equivalent to the earlier approach.

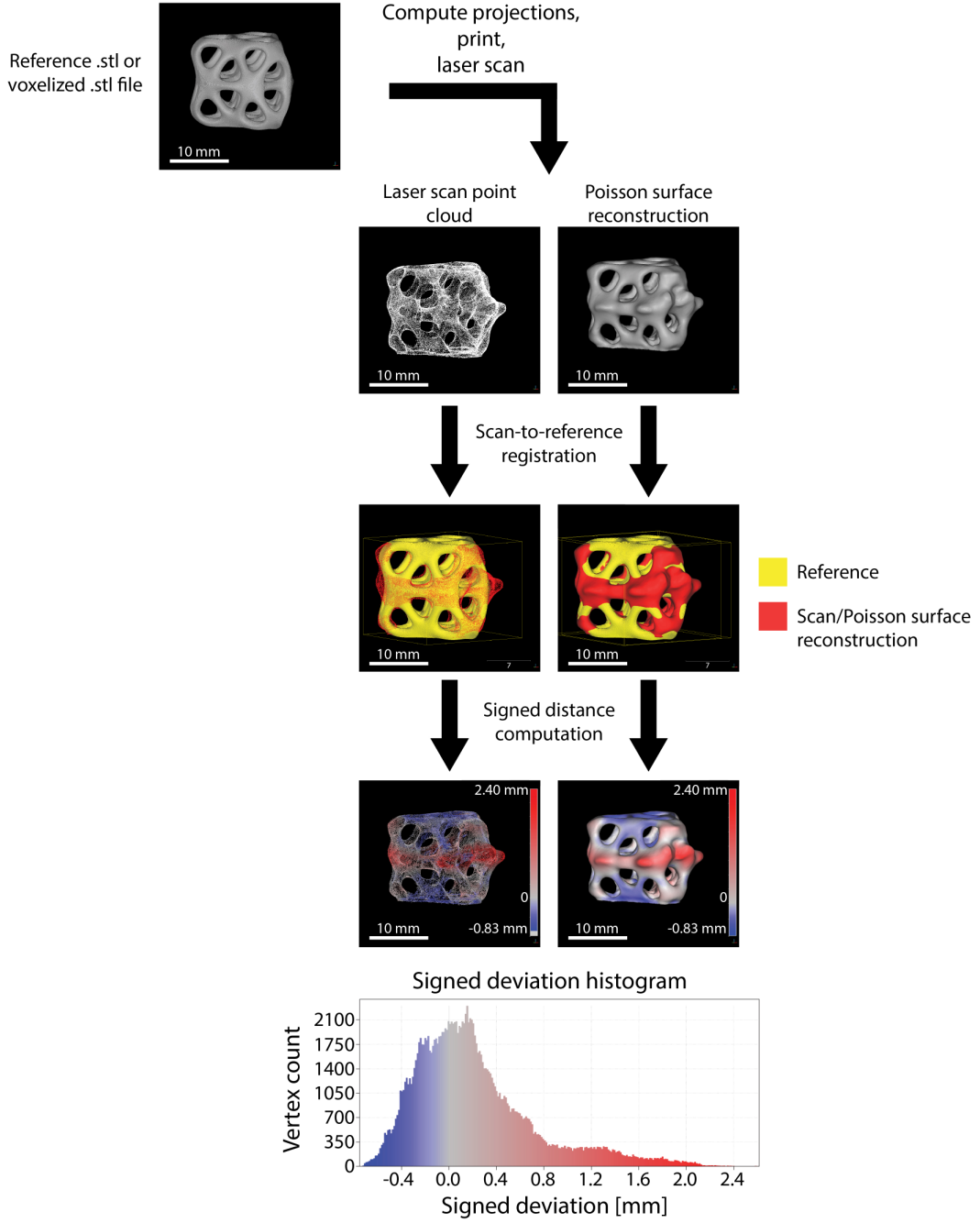


Figure S2: VAM metrology methodology using CloudCompare point cloud software. The reference (to-be-printed) .stl file is used to generate and optimize projections. The CAL 3D print is completed and the post-processed part is laser scanned. The scan point cloud is loaded and its global position is registered to the reference voxelated .stl surface. The scan point cloud may be used directly without modification or to create a Poisson surface reconstruction for analysis. Then, the signed deviation between the two surfaces (laser-scanned surface and reference surface) is computed and the data is plotted on a histogram and colormap on the analyzed surface for compact visualization of the print fidelity.

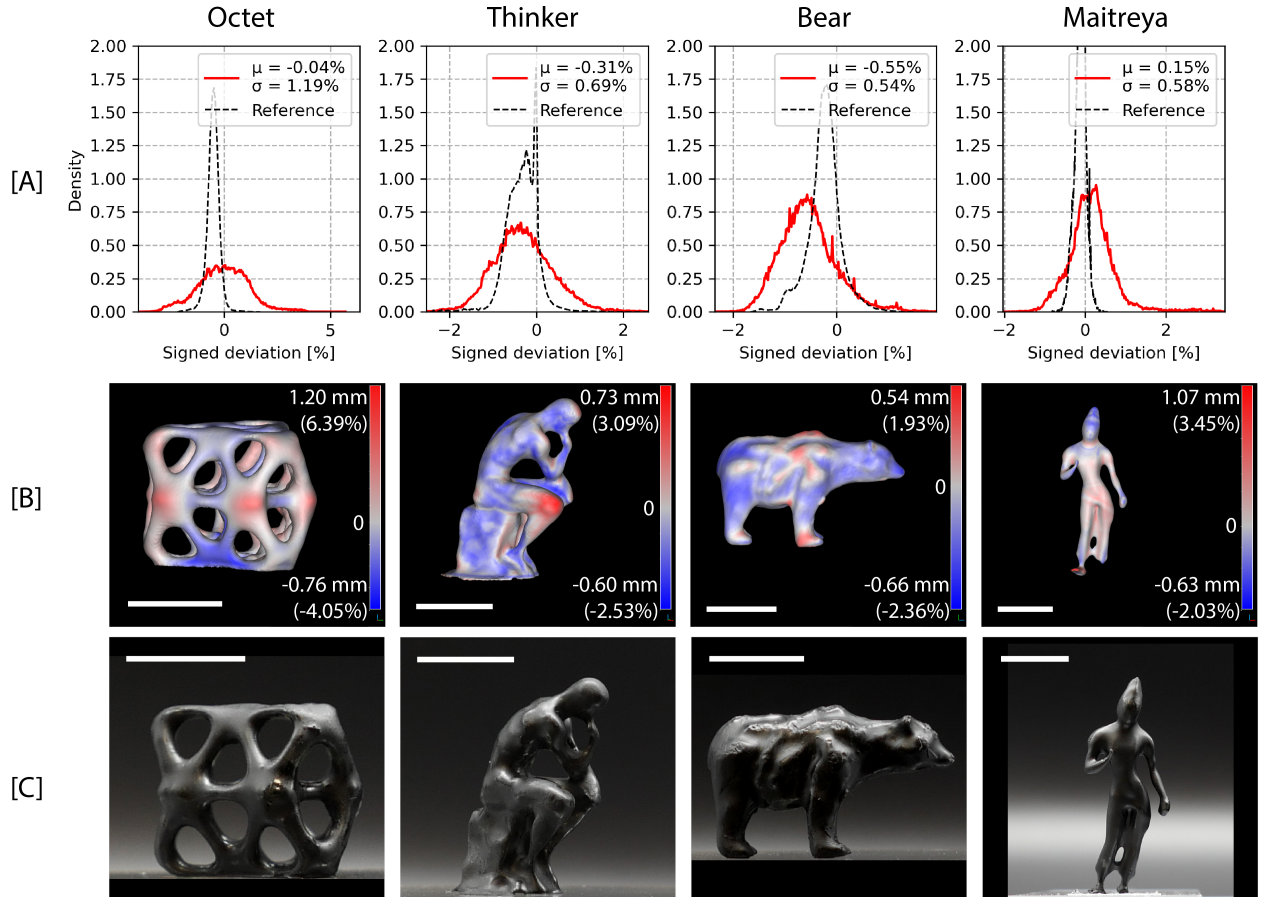


Figure S3: Laser scanning measurement of all PM-optimized geometries compared to reference geometries: [A] signed deviation histograms (red) comparing laser scan surface to target geometry, normalized to a percentage of the maximum bounding box dimension of the underlying target geometry. The reference histogram (dashed black) shows the comparison of the simulated prints at the optimal threshold for peak mIoU to the target geometry (Fig. 4[C]). [B] Laser-scanned 3D surface with signed deviation colormap where red indicates laser-scanned surface lies outside the target surface and blue indicates the laser-scanned surface lies inside the target surface. [C] Photographs of printed and scanned geometries. Note: printed parts are painted black to reduce reflectivity and improve laser scannability. Scale bars = 10 mm.

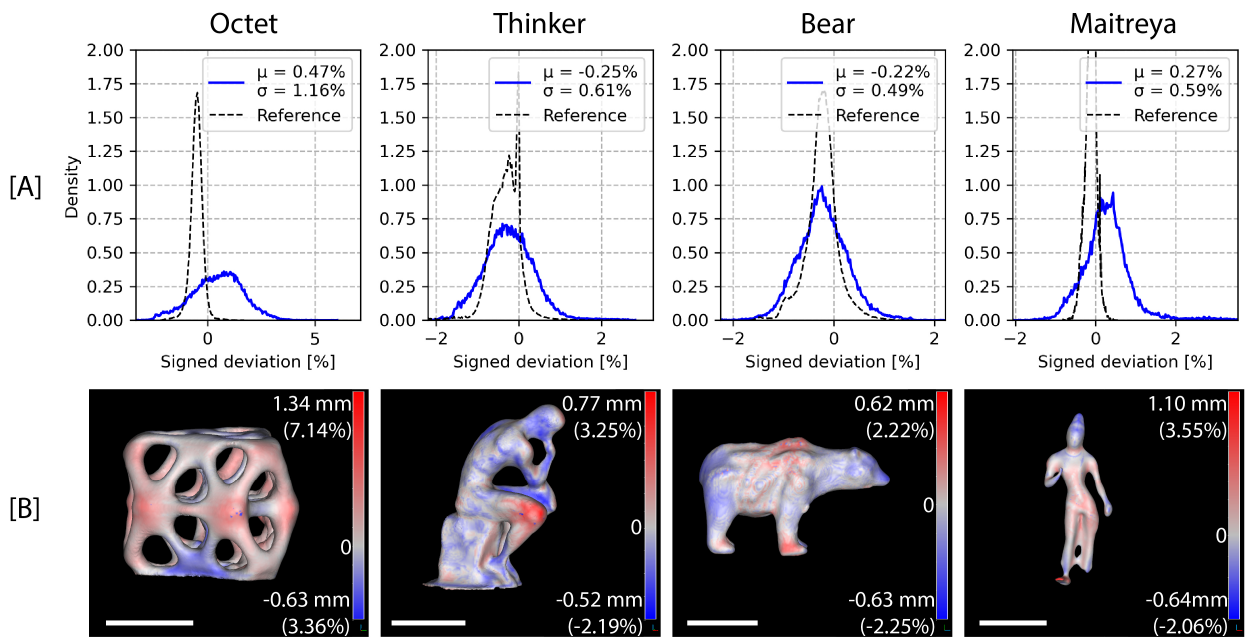


Figure S4: Laser scanning measurement of all PM-optimized geometries compared to best simulated geometries using filtered initialization: [A] signed deviation histograms (blue) comparing laser scan surface to the PM best simulated surface geometry, normalized to a percentage of the maximum bounding box dimension of the underlying target geometry. The reference histogram (dashed black) shows the comparison of the simulated prints at the optimal threshold for peak mIoU to the target geometry (Fig. 4[C]). [B] Laser-scanned 3D surface with signed deviation colormap where red indicates the laser-scanned surface lies outside the simulated surface and blue indicates the laser-scanned surface lies inside the simulated surface. Scale bars = 10 mm.

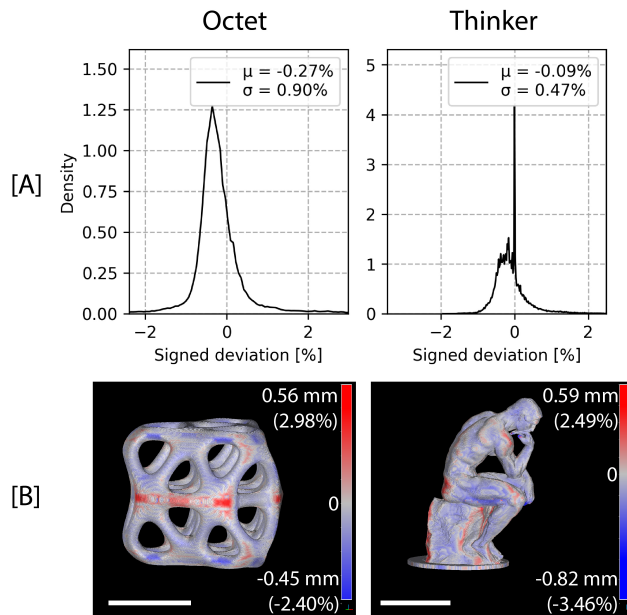


Figure S5: DM-optimized simulated signed deviation: [A] signed deviation histograms comparing best simulated surface geometry using filtered initialization to target geometry, [B] voxelated target surface plotted with colormap of the signed deviation to the DM best simulated surface, where red indicates the simulated surface lies beyond the outside the target surface and blue indicates the simulated surface lies inside the target surface (see Section 4 for more details). Octet  $3\sigma = 0.51$  mm and Thinker  $3\sigma = 0.33$  mm. Scale bars = 10 mm.

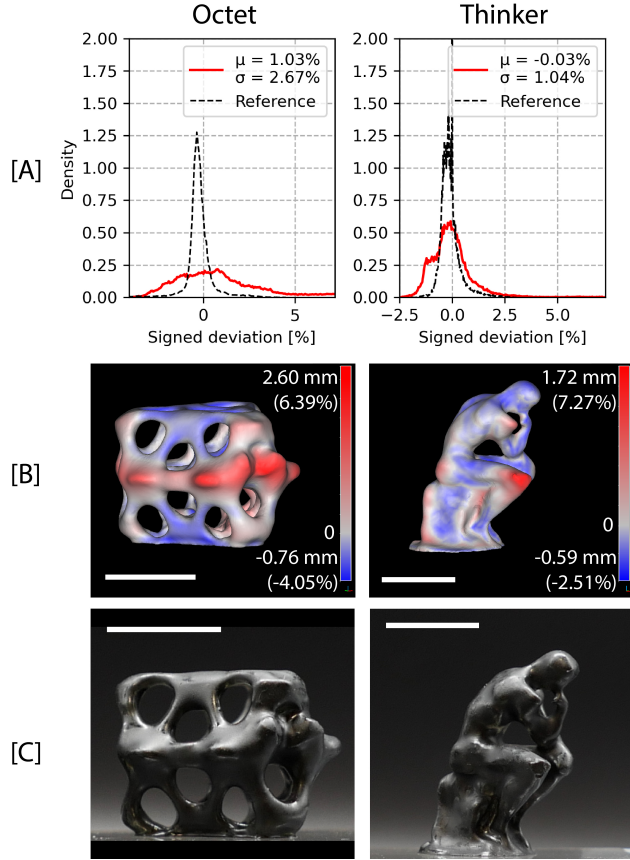


Figure S6: Laser scanning measurement of both DM-optimized geometries compared to reference geometries: [A] signed deviation histograms (red) comparing laser scan surface to target geometry, normalized to a percentage of the maximum bounding box dimension of the underlying target geometry. The reference histogram (dashed black) shows the comparison of the simulated prints at the optimal threshold for peak mIoU to the target geometry (Fig. 4[C]). [B] Laser-scanned 3D surface with signed deviation colormap where red indicates the laser-scanned surface lies outside the target surface and blue indicates the laser-scanned surface lies inside the target surface. [C] Photographs of printed and scanned geometries. Note: printed parts are painted black to reduce reflectivity and improve laser scannability. Scale bars = 10 mm.

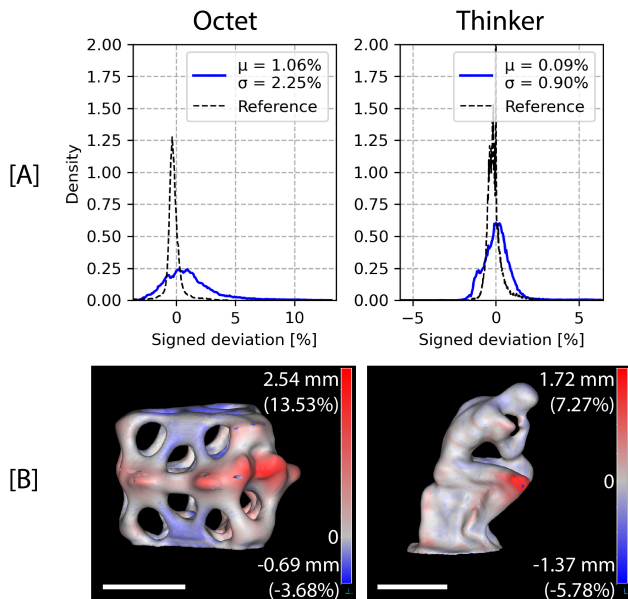


Figure S7: Laser scanning measurement of DM-optimized geometries compared to best simulated geometries using filtered initialization: [A] signed deviation histograms (blue) comparing laser scan surface to the DM best simulated surface geometry, normalized to a percentage of the maximum bounding box dimension of the underlying target geometry. The reference histogram (dashed black) shows the comparison of the simulated prints at the optimal threshold for peak mIoU to the target geometry (Fig. 4[C]). [B] Laser-scanned 3D surface with signed deviation colormap where red indicates the laser-scanned surface lies outside the simulated surface and blue indicates the laser-scanned surface lies inside the simulated surface. Scale bars = 10 mm.